PAPER • OPEN ACCESS

Direct laser cooling of calcium monohydride molecules

New Journal of Physics
The open access journal at the forefront of physics

Deutsche Physikalische Gesellschaft DPG
IOP Institute of Physics

Published in partnership with: Deutsche Physikalische Gesellschaft and the Institute of Physics

OPEN ACCESS

RECEIVED
9 March 2022

REVISED
28 June 2022

ACCEPTED FOR PUBLICATION
12 July 2022

PUBLISHED
9 August 2022

PAPER

Direct laser cooling of calcium monohydride molecules

S F Vázquez-Carson, Q Sun, J Dai, D Mitra* and T Zelevinsky

Department of Physics, Columbia University, New York, NY 10027-5255, United States of America
* Author to whom any correspondence should be addressed.

E-mail: dm3710@columbia.edu and tanya.zelevinsky@columbia.edu

Keywords: laser cooling, diatomic molecule, calcium monohydride, Sisyphus cooling, optical cycling, vibrational branching ratio, precision measurement

Abstract

We demonstrate optical cycling and laser cooling of a cryogenic buffer-gas beam of calcium monohydride (CaH) molecules. We measure vibrational branching ratios for laser cooling transitions for both excited electronic states A and B. Furthermore, we measure that repeated photon scattering via the $A \leftarrow X$ transition is achievable at a rate of $\sim 1.6 \times 10^6$ photons s^{-1} and demonstrate interaction-time limited scattering of $\sim$200 photons by repumping the largest vibrational decay channel. We also demonstrate a sub-Doppler cooling technique, namely the magnetically assisted Sisyphus effect, and use it to cool the transverse temperature of a molecular beam of CaH. Using a standing wave of light, we lower the transverse temperature from 12.2(1.2) mK to 5.7(1.1) mK. We compare these results to a model that uses optical Bloch equations and Monte Carlo simulations of the molecular beam trajectories. This work establishes a clear pathway for creating a magneto-optical trap (MOT) of CaH molecules. Such a MOT could serve as a starting point for production of ultracold hydrogen gas via dissociation of a trapped CaH cloud.

1. Introduction

The development of robust techniques for laser cooling of atoms [1, 2] has led to major advancements in the fields of quantum simulation, quantum computation, and frequency metrology, and has enabled precise tests of fundamental physics [3–6]. Cooling and trapping of molecules represents the next level in experimental complexity because of the additional internal degrees of freedom and the lack of perfect two-level structure that can be used for sustained photon cycling [7]. In exchange for this increase in complexity, molecules provide enhanced sensitivity for fundamental precision measurements [8–10], long coherence times for quantum information [11–13], and tunable long-range interactions for quantum simulators [12, 14]. The technique of buffer gas cooling [15, 16] has enabled direct laser cooling of molecules, including several diatomic [17–21], triatomic [10, 22, 23], and symmetric top [24] species. We add the alkaline-earth-metal calcium monohydride (CaH) to this growing list.

A cold and trapped cloud of hydrogen atoms promises to be an ideal system for testing quantum electrodynamics and precise measurements of fundamental constants [25, 26]. More than two decades ago, a BEC of atomic hydrogen was prepared in a magnetic trap [27]. The measurement of the 1S–2S transition has been performed in a magnetic trap of hydrogen [28] and antihydrogen [29] and also in a beam [30]. More recently, experiments measured the 1S–3S [31] and the $2S_{1/2}$–$8D_{5/2}$ [32] transitions of hydrogen with unprecedented precision. Furthermore, magnetic slowing of paramagnetic hydrogen has been proposed [33]. While extremely successful, these experiments are often limited by motional effects. Performing measurements with dilute ultracold samples of hydrogen tightly trapped in an optical potential could improve the precision.

A possible pathway to such samples is via fragmentation of hydride molecules [34] and ions [35]. Diatomic hydride radicals can be efficiently cooled using direct laser cooling techniques. Additionally, if the controlled fragmentation process does not heat the sample, the resulting hydrogen atoms can populate a Boltzmann distribution at a lower temperature than the parent molecules. This presents barium

monohydride as an ideal candidate where the large mass difference between the barium atom and the hydrogen atom could result in an ultracold cloud of hydrogen atoms after fragmentation [34]. Although BaH was successfully laser cooled [21], its low recoil momentum and a relatively weak radiation pressure force make it challenging to load into a magneto-optical trap (MOT).

In this work, we explore an alternative molecule for laser cooling and trapping, CaH. Due to its diode-laser accessible transitions and short excited state lifetimes, CaH is a promising candidate for optical cycling. Indeed CaH was among the earliest molecules proposed for laser cooling [36]. In addition, buffer gas cooling [37], magnetic trapping and evaporative cooling [38] of CaH have been demonstrated. Here we show direct laser cooling of CaH. In section 2 we describe the electronic structure and relevant optical transitions for this molecule. We also characterize our cryogenic buffer gas beam source. In section 3 we summarize the measurement of the vibrational branching ratios (VBRs) for this molecule and establish a photon budget for laser cooling. In section 4 we present the measurement of the photon scattering rate and show that we can achieve rates over 10^6 photons s^{-1}. In section 5 we demonstrate an ability to cool a beam of CaH via a sub-Doppler technique by a factor of ∼2 in one dimension while only scattering ∼140 photons. Finally, in section 6 we conclude that these results establish CaH as a promising candidate for laser cooling and trapping.

2. Experimental setup

The experiment consists of a cryogenic buffer gas beam source operating at ∼6 K [15, 16, 21]. We employ ^{4}He as a buffer gas that is flowed into the cell at a rate of ∼6 sccm (standard cubic centimeter per minute) via a capillary on the back of the cell (figure 1(a)). The target is composed of pieces of CaH_2 (Sigma-Aldrich, 95% purity) held on a copper stub using epoxy. To ablate the target, we use the fundamental output of an Nd:YAG pulsed laser operating at 1064 nm and at a 2 Hz repetition rate. We run the ablation laser at a maximum pulse energy of 30 mJ and focus the beam to a diameter of 1.5 mm. We observe the highest molecular yield when the ablation energy is deposited over a large target surface area. The CaH radicals produced due to ablation subsequently thermalize their internal rotational and vibrational degrees of freedom via collisions with the buffer gas. These molecules are then hydrodynamically entrained in the buffer gas flow out of the cell. The molecules leaving the cell are predominantly in the lowest two rotational states ($N'' = 0$ and 1) and the ground vibrational state ($\nu'' = 0$).

After leaving the cryostat, the molecules enter a high vacuum chamber equipped with a beam aperture of 5 mm diameter to filter out the $1/e^2$ transverse velocity range to $\sim \pm 3$ m s^{-1} (figure 1(a)). We keep the aperture in place for all data shown in this work. Subsequently, the molecules enter an interaction region with rectangular, antireflection coated windows enabling a 12 cm long interaction length. Next, the molecules enter a 'cleanup' region, where population accumulated in the $X(\nu'' = 1)$ state is pumped back to the $X(\nu'' = 0)$ state via the $B(\nu' = 0)$ state, and are then detected in the imaging region by scattering photons on the $B(\nu' = 0) \leftarrow X(\nu'' = 0)$ transition. The scattered photons are simultaneously collected on a photon counting photo-multiplier tube (PMT) and an electron-multiplying charge-coupled device (EMCCD) camera. An example of the average camera images collected is shown in figure 1(b).

The relevant energy level structure for CaH is depicted in figure 1(c). We start in the ground electronic manifold ($X^2\Sigma^+$) and excite to the two lowest excited electronic states ($A^2\Pi_{1/2}$ and $B^2\Sigma^+$). A rotationally closed optical cycling transition can be guaranteed by selection rules if we address the $N'' = 1, J'' = 1/2, 3/2$ ground states to the opposite parity $J' = 1/2$ excited state in the A manifold or the $N' = 0$ state in the B manifold [39]. The ground $X(N = 1)$ state is split into two components separated by 1.86 GHz due to the spin-rotation interaction (figure 1(d)). Each sublevel is further split into two hyperfine sublevels ($J = 1/2, F = 0, 1$ and $J = 3/2, F = 1, 2$) separated by 54 MHz and 101 MHz respectively. Each hyperfine sublevel is composed of $2F + 1 m_F$ states that remain unresolved for the purpose of this study. The hyperfine splitting of the excited A and B states of interest ($J = 1/2$) is not resolved. The primary vibrational decay from both A and B excited states is to the $\nu'' = 1$ state (∼1%–3%) and subsequently to the $\nu'' = 2$ state (<0.3%). For this work, we only repump the population out of the $\nu'' = 1$ state. The details of the laser setup can be found in appendix A.

We estimate the longitudinal velocity of our molecular beam as follows. Every ablation pulse produces Ca atoms that get buffer gas cooled and extracted from the cell alongside the CaH molecules. We measure the longitudinal velocity profile of these Ca atoms within the cleanup region, 92 cm from the cell aperture, by addressing the $^1S_0 \rightarrow {}^1P_1$ transition in calcium at 423 nm in a velocity sensitive configuration (laser $\vec{k}$ is at 70° relative to the beam's forward velocity vector). The high density of calcium in the beam allows us to measure the Doppler-shifted atomic resonance with a high signal-to-noise ratio. We find that the longitudinal velocity is peaked at ∼250 m s^{-1} with a full width at half maximum of ∼200 m s^{-1}. Since the

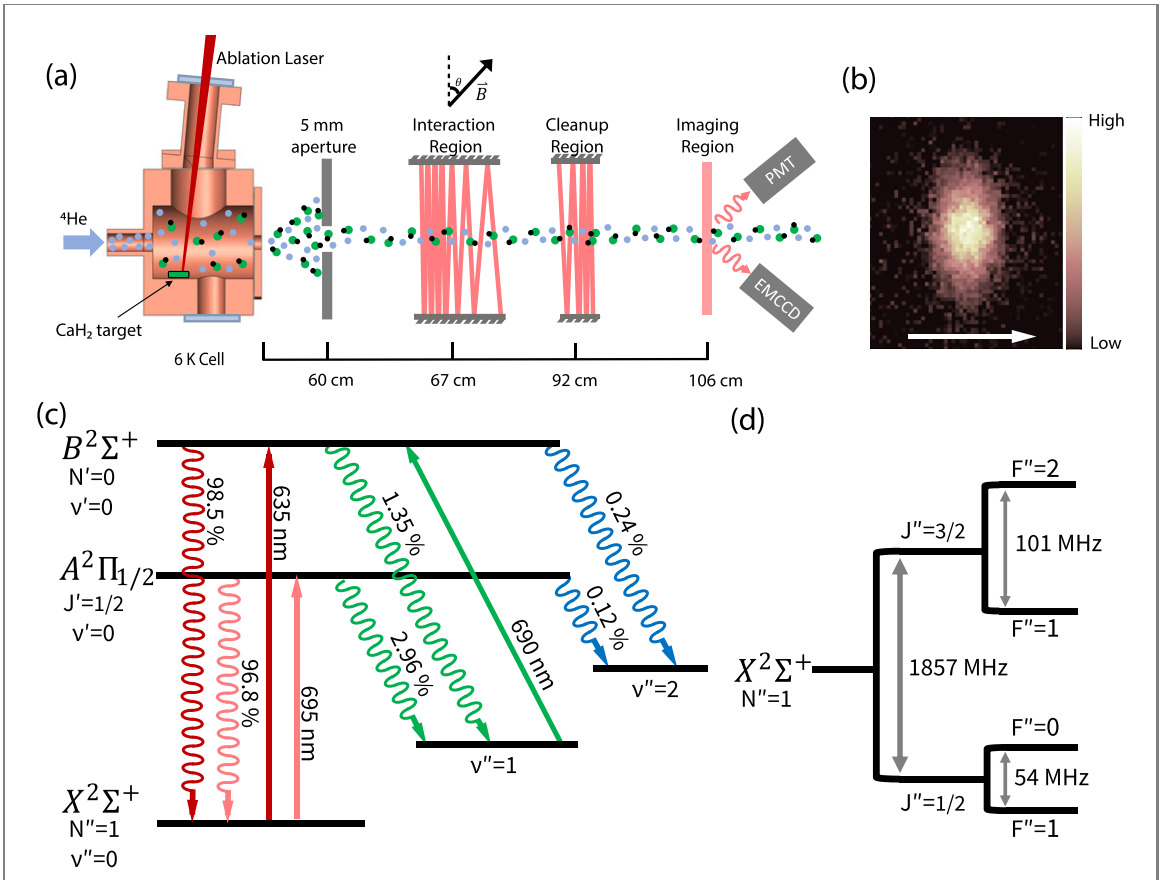

Figure 1. Experimental setup and molecular structure. (a) Experiment diagram (not to scale). CaH molecules and Ca atoms are produced via ablation of a solid target of CaH_2. The ejected molecules thermalize to the ∼6 K ^{4}He buffer gas and are extracted through a 3 mm diameter aperture. An additional 5 mm aperture is placed just before the molecular beam enters the interaction region to limit the transverse velocity distribution. The cooling chamber consists of 12 cm of optical access followed by a cleanup region and a detection region. (b) A sample image of molecules in the beam taken with the EMCCD camera. Photons are collected for 7 ms during imaging. Arrow indicates the direction of the molecular beam. (c) The main cooling line used in this work is the $A^2\Pi_{1/2}(\nu' = 0, J' = 1/2) \leftarrow X^2\Sigma^+(\nu'' = 0, N'' = 1)$ transition at 695 nm. We detect the molecular beam using the $B^2\Sigma^+(\nu' = 0, N' = 0) \leftarrow X^2\Sigma^+(\nu'' = 0, N'' = 1)$ transition using 2.6 W cm^{-2} of 635 nm light. We employ laser light at 690 nm to repump molecules that decay to the $\nu'' = 1$ vibrational state in X by addressing the $B^2\Sigma^+(\nu' = 0, N' = 0) \leftarrow X^2\Sigma^+(\nu'' = 1, N'' = 1)$ transition. By closing this leak, we create a quasi-closed transition capable of cycling ∼200 photons sufficient to exert a measurable Sisyphus force. (d) The 1.86 GHz spin-rotation splitting and the 54 MHz (101 MHz) hyperfine structure of the $J = 1/2(J = 3/2)$ states in the ground X manifold. The details of the laser setup can be found in appendix A.

masses of CaH and Ca are nearly identical and they experience identical buffer-gas cooling, we assign the same longitudinal velocity profile to both species. We also estimate the molecular beam flux in our system via the total camera counts and the estimated collection efficiency of the imaging system (see appendix B for details). We obtain a typical beam flux of $\sim 1 \times 10^{10}$ molecules/steradian/pulse.

3. Vibrational branching ratio measurement

Although the cycling transition in CaH is rotationally closed, no selection rules prevent vibrational decay. The probability of decay from the excited electronic state to vibrationally excited X states is quantified by the VBR. To reduce the number of repumping lasers required to scatter $\sim 10^5$ photons, it is essential that the off-diagonal VBRs are highly suppressed [36, 39]. The directly laser cooled diatomic molecules to date, including CaF [18, 19], SrF [40], YbF [41] and YO [20], all possess highly diagonal transitions. The Franck–Condon factor (FCF) is defined as the square of the wavefunction overlap for two different vibrational states which is typically obtained from *ab initio* calculations. The conversion between VBRs (denoted as q) and FCFs (denoted as f) can be derived from the Einstein A coefficient [42] and is given by

$$q_{\nu'\nu''} = \frac{f_{\nu'\nu''} \times \omega^3_{\nu'\nu''}}{\sum_{n=0}^{\infty} f_{\nu' n} \times \omega^3_{\nu' n}}, \tag{1}$$

where $\omega_{\nu'\nu''}$ is the positive energy difference between the states ν' and ν''. The above expression assumes that the radial variation of the transition dipole moment is negligible, which is a reasonable approximation

Table 1. FCFs and VBRs for the measured transitions of CaH. The experimental radiative lifetime for the A state was obtained from reference [49] and for the B state from reference [50]. The excited state vibrational quantum number is always $\nu' = 0$. The $A(\nu' = 0) \leftarrow X(\nu'' = 0)$ excitation wavelength at 695.13 nm, the $B(\nu' = 0) \leftarrow X(\nu'' = 0)$ excitation wavelength at 635.12 nm, and the $B(\nu' = 0) \leftarrow X(\nu'' = 1)$ excitation wavelength at 690.37 nm were determined experimentally. The other transition wavelengths are derived using measured vibrational energies given in reference [51]. The calculated FCFs are obtained from [43] for the $A \rightarrow X$ decay and from [46] for the $B \rightarrow X$ decay. Error bars for the measured FCFs and VBRs are statistical standard errors.

Transition	Lifetime τ (ns)	Vibrational quanta (ν'')	Transition wavelength (nm)	FCF theory ($f_{0\nu''}$)	FCF measured ($f_{0\nu''}$)	VBR measured ($q_{0\nu''}$)
$A \rightarrow X$	33(3)	0	695.13	0.953	0.9572(43)	0.9680(29)
		1	761.87	0.0439	0.0386(32)	0.0296(24)
		2	840.07	2.74×10^{-3}	$4.2(3.2) \times 10^{-3}$	$2.4(1.8) \times 10^{-3}$
		3	932.80	2.3×10^{-4}	—	—
$B \rightarrow X$	58(2)	0	635.12	0.9856	0.9807(13)	0.9853(11)
		1	690.37	0.0132	0.0173(13)	0.0135(11)
		2	753.97	1.1×10^{-3}	$2.0(0.3) \times 10^{-3}$	$1.2(0.2) \times 10^{-3}$
		3	827.84	1×10^{-4}	—	—

within our measured precision. Alkaline-earth monohydrides have been extensively studied and FCFs have been calculated or measured for BeH, MgH, SrH and BaH [43–46]. Calculated values for CaH [43, 46, 47] are summarized in table 1. In this section we report our measurement of VBRs for the $A(\nu' = 0)$ and $B(\nu' = 0)$ states of CaH, denoted by $q_{0,\nu''}$ where ν'' is 0, 1 and 2.

We perform the VBR measurement with our molecular beam using a process similar to the one described in reference [48]. A pump laser beam intersects the CaH beam orthogonally in the imaging region, and resonantly excites the molecules from $X^2\Sigma^+(\nu'' = 0)$ ground states to the $A^2\Pi_{1/2}(\nu' = 0)$ or $B^2\Sigma^+(\nu' = 0)$ excited states. Once excited, two PMTs in photon-counting mode with different dichroic filters are used to collect the photons simultaneously emitted from the various decay pathways of the excited state. The narrow bandpass dichroic filters are strategically chosen to isolate photons with a frequency resonant with vibrational decay to a single excited vibrational state ($\lambda_{0\nu''}$) while simultaneously detecting the molecules that return to the ground state (λ_{00})[1].

We first compare the time traces of two PMTs when their filters allow transmission at the same λ_{00} frequency. The ratio of integrated signals, R_0, can be expressed with systematic parameters and VBRs as

$$R_0 = \frac{N q_{00} \Omega_{P_2} T_{F_2,\lambda_{00}} Q_{P_2,\lambda_{00}}}{N q_{00} \Omega_{P_1} T_{F_1,\lambda_{00}} Q_{P_1,\lambda_{00}}}, \tag{2}$$

where the subscripts P_1/P_2 stand for two PMTs used in this experiment[2], subscripts F_1/F_2 stand for the two bandpass filters used, N is the number of scattering events, q_{00} is the diagonal VBR, Ω_P is the geometrical collection efficiency for a given PMT, $T_{F,\lambda}$ is the transmission efficiency for a given bandpass filter at a wavelength λ, and $Q_{P,\lambda}$ is the quantum efficiency for a given PMT at a wavelength λ.

Next, we replace filter F_2 with another filter F_3 which blocks transmission at λ_{00} and allows transmission at $\lambda_{0\nu''}$, where ν'' is 1 or 2. The ratio of integrated signals, $R_{\nu''}$, can then be written as

$$R_{\nu''} = \frac{N' q_{0\nu''} \Omega_{P_2} T_{F_3,\lambda_{0\nu''}} Q_{P_2,\lambda_{0\nu''}}}{N' q_{00} \Omega_{P_1} T_{F_1,\lambda_{00}} Q_{P_1,\lambda_{00}}}. \tag{3}$$

An example of the measured signals is shown in figure 2(a). For each measurement we simultaneously collect the time traces from the two PMTs. In order to obtain the ratio $R_{\nu''}$, we perform a one-parameter least square fit of all points in one time trace to the other (figure 2(a) inset). Since the PMTs are stationary throughout the experiment, any variation in Ω is negligible. By measuring the transmission efficiency of the filters F_2/F_3 at $\lambda_{00}/\lambda_{0\nu''}$, as well as the quantum efficiency of P_2 at $\lambda_{00}/\lambda_{0\nu''}$, and combining equations (2) and (3), we estimate the ratio of VBRs as

$$\frac{q_{0\nu''}}{q_{00}} = \frac{R_{\nu''} Q_{P_2,\lambda_{00}} T_{F_2,\lambda_{00}}}{R_0 Q_{P_2,\lambda_{0\nu''}} T_{F_3,\lambda_{0\nu''}}}. \tag{4}$$

We calculate the individual VBRs by assuming that the sum is $\sum_{\nu''=0}^{2} q_{0\nu''} = 1$. This is a reasonable approximation since the calculated value of f_{03} is smaller than the statistical uncertainty in the measured

[1] A complete list of filters used in this experiment and their measured transmission efficiencies at certain wavelengths can be found in appendix C.

[2] PMTs used: Hamamatsu R13456 and SensTech P30PC-01.

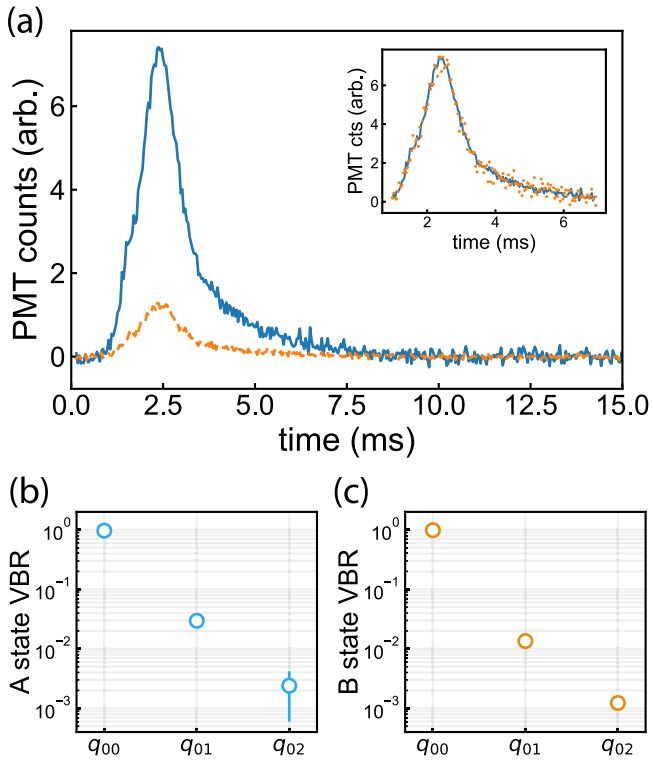

Figure 2. Measurement of the VBRs for CaH molecules. (a) An example of PMT traces used to calculate the VBRs. These two time traces correspond to background-subtracted fluorescence from the decay to $X(\nu'' = 0)$ for PMTs P_1 (orange, dashed) and P_2 (blue, solid) while the $B^2\Sigma^+(\nu' = 0) \leftarrow X^2\Sigma^+(\nu'' = 0)$ transition is excited. Due to a different operating configuration, the molecular beam velocity is ∼400 m s^{-1} for this data. The inset denotes how the ratio of integrated signals, R_0, is computed. We perform a one-parameter fit of the dashed trace to the solid trace. The result of the fit produces the orange points that can be seen to overlap temporally with the blue trace. (b) and (c) The resulting VBRs from the measured ratio $R_{\nu''}$, obtained by evaluating equation (4), for the A and B states. Each point represents an average of at least 200 shots with background subtraction, while the higher vibrational decays require ∼700 shots for an appreciable signal-to-noise ratio due to the low probability of decaying to these excited states. Error bars are statistical standard errors.

FCFs for both A and B states (table 1). The resulting VBRs are plotted in figures 2(b) and (c). The measured FCFs were calculated using the inverted form of equation (1).

4. Scattering rate measurement

Efficient cooling and slowing of molecules require rapid scattering of photons while simultaneously minimizing the loss to unaddressed vibrationally excited states. From the measured VBRs for the primary decay pathways for CaH as described in section 3, we obtain the average number of photons per molecule, $\langle N_{\mathrm{ph}} \rangle$, that we expect to scatter while addressing N_{v} vibrational channels before only $1/e$ of the ground state population remains available for optical cycling as

$$\langle N_{\mathrm{ph}} \rangle \simeq \frac{1}{1 - \sum_{\nu''=0}^{N_{\mathrm{v}}} q_{0\nu''}}. \tag{5}$$

Thus we expect to scatter 31(3) photons for $A \leftarrow X(\nu'' = 0)$ and 68(5) photons for $B \leftarrow X(\nu'' = 0)$ before losing 63% of molecules to the $X(\nu'' = 1)$ state. Next, if the $X(\nu'' = 1)$ state is repumped, this photon number increases to around 400 for the A state and 800 for the B state cycling schemes. In order to slow a CaH molecule travelling at 250 m s^{-1} to within the capture velocity of a MOT [19, 21], we would need to scatter $\sim 2 \times 10^4$ photons. Although the loss to excited vibrational modes can be minimized by using repumping lasers for higher vibrational states, it is essential to scatter photons at a high rate so that the slowing distance can be minimized. The maximum scattering rate for a multilevel system with n_{g} ground states and n_{e} excited states is given by [52]

$$R_{\mathrm{sc,max}} = \Gamma_{\mathrm{eff}} = \frac{1}{\tau} \frac{n_{\mathrm{e}}}{n_{\mathrm{e}} + n_{\mathrm{g}}}, \tag{6}$$

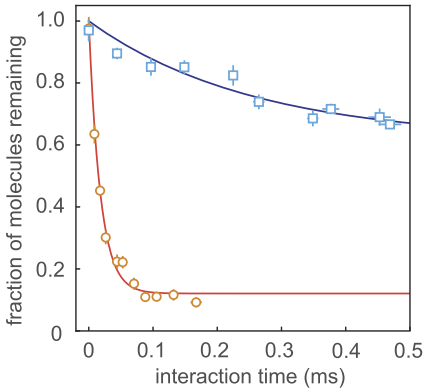

Figure 3. Scattering rate measurement. The fraction of molecules remaining in the $X(\nu'' = 0)$ state when cycling on the $A(\nu' = 0) \leftarrow X(\nu'' = 0)$ transition (orange circles) and the fraction remaining in $X(\nu'' = 0) + X(\nu'' = 1)$ states when cycling simultaneously on the $A(\nu' = 0) \leftarrow X(\nu'' = 0)$ and the $B(\nu' = 0) \leftarrow X(\nu'' = 1)$ transitions (blue squares) are measured as a function of the interaction time. Lines are fits to exponential decay curves with finite offsets. The offset is due to detected molecules that are only weakly addressed in the interaction region. The exponential decay time constant τ_d from the fit is $5.5(3) \times 10^4$ s^{-1} for the orange curve and $3.92(13) \times 10^3$ s^{-1} for the blue curve.

where τ is the excited state lifetime given in table 1. The rotationally closed transition employed here is $N' = 0 \leftarrow N'' = 1$, i.e., $n_e = 4$ and $n_g = 12$ (see figure 1(d)). Here we assume that the repumping lasers couple to different excited states. We obtain the maximum scattering rate $\sim 7.6 \times 10^6$ s^{-1} for the A state and $\sim 4.3 \times 10^6$ s^{-1} for the B state. In practice, however, it is difficult to achieve these maximum values and most experiments with diatomic, triatomic, and polyatomic molecules to date achieve scattering rates up to $\sim 2 \times 10^6$ s^{-1}.

In order to determine the maximum scattering rate achievable in our setup, we measure the fraction of molecules that are pumped to dark vibrationally excited states as a function of interaction time. First, we apply only the $A \leftarrow X(\nu'' = 0)$ linearly polarized, resonant light ($\sim$80 mW per spin-rotation component) in the interaction region in a multi-pass configuration (figure 1(a)). Each pass of the laser beam is spatially resolved so that the effective interaction length can be varied and quantified by counting the number of passes. We detect the population remaining in $X(\nu'' = 0)$, and we convert the interaction length to time by measuring the laser beam waist ($1/e^2$ radius of 0.55 mm in the direction parallel to the molecular beam and 0.84 mm in the orthogonal direction) and estimating the average velocity weighted by the relative population within the velocity distribution (251 m s^{-1}). We also apply a 3 G magnetic field in the interaction region to destabilize the dark magnetic sublevels that become populated during optical cycling. Magnetic field strength and laser polarization angle with respect to the magnetic field are scanned to maximize the scattering rate. The angle between the magnetic field and the polarization of the laser that addresses $A \leftarrow X(J = 3/2, F = 2)$ was ultimately chosen to be $\sim 13^\circ$.

As the molecules propagate through the interaction region and scatter photons, some of the excited state molecules decay to unaddressed higher vibrational states at a rate given by the sum of addressed state VBRs as

$$f_{\mathrm{rem}}(t) = \frac{N_{\mathrm{mol}}(t)}{N_{\mathrm{mol}}(t=0)} = \left(\sum_{\nu''=0}^{\nu_a} q_{0\nu''}\right)^{N_p(t)} \tag{7}$$

where f_{rem} is the fraction of molecules that remain in all the addressed states combined. The number of scattered photons is $N_p(t) = R_{sc}t$, and ν_a is the highest addressed vibrational level. The experimental data is shown in figure 3 (orange circles). We fit the decay in f_{rem} to an exponential decay with a finite offset. We note that in the limit of infinite interaction time, $f_{\mathrm{rem}} \to 0$. However, in our setup we have a small fraction of the molecules that only weakly interact with the laser beam but are still detected in the imaging region. These molecules are accounted for by adding a constant offset to f_{rem}. From the exponential decay constant τ_d, we can obtain the scattering rate

$$R_{sc} \simeq \frac{1}{\tau_d\left(1 - \sum_{\nu''=0}^{\nu_a} q_{0\nu''}\right)}. \tag{8}$$

Using our measured values of the VBRs and τ_d from the orange curve of figure 3, we estimate an average scattering rate of $1.67(15) \times 10^6$ s^{-1}. Here we make a simplifying assumption that the local variation in

light intensity does not affect our estimate. We justify this assumption by noting that the laser intensity far exceeds the predicted saturation intensity ($I_{\mathrm{sat}} \approx 1.9$ mW cm^{-2}) after accounting for the Gaussian laser beam profile, beam propagation, and power loss per pass.

Next, we measure R_{sc} after adding ∼110 mW of repumping light addressing the $B(\nu' = 0) \leftarrow X(\nu'' = 1)$ transition, co-propagating with the main cooling light. In this case, we also add ∼40 mW of the same repumping light to the cleanup region. Within this multi-pass cleanup region, we are able to transfer the $X(\nu'' = 1)$ population to $X(\nu'' = 0)$ with >90% efficiency. The resulting data is plotted in figure 3 (blue squares). In this case the decay time is much longer, since it takes 33 photons for a $1/e$ decay in ground state population when only the $A(\nu' = 0) \leftarrow X(\nu'' = 0)$ is addressed, while it takes ∼400 photons when the repump is added. However, the precision of this experiment is limited by the measured VBR values from section 3. From the decay constant of the exponential fit, we obtain an average scattering rate $1.6(1.2) \times 10^6$ s^{-1}. The uncertainty mostly comes from the VBR value q_{02}. Nevertheless, the two independent measurements provide an order-of-magnitude estimate of the scattering rate. The relatively high values of R_{sc} indicate that we can achieve sufficiently high scattering rates for CaH molecules. Finally, at the longest interaction time, we estimate that 170^{+500}_{-70} photons per molecule are scattered.

5. Magnetically assisted Sisyphus cooling

The techniques of radiative slowing and magneto-optical trapping rely on the Doppler mechanism, where the scattering rate is optimized when the laser detuning matches the Doppler shift of the molecular transition ($\delta = \vec{k} \cdot \vec{v}$). However, Doppler cooling is fundamentally limited by the excited state lifetime to a temperature of $T_{\mathrm{D}} = \hbar/(2k_{\mathrm{B}}\tau)$, which is known as the Doppler temperature. For CaH cooled on the $A \leftarrow X$ transition, we estimate $T_{\mathrm{D}} = 116$ μK. Hence in order to achieve temperatures below this limit, sub-Doppler cooling techniques must be implemented [18, 53–55]. Here we demonstrate the ability to perform a type of sub-Doppler cooling known as magnetically assisted Sisyphus cooling in one dimension.

The technique of Sisyphus cooling was first demonstrated with atoms [56, 57]. It was subsequently demonstrated with diatomic [17, 41], triatomic [22], and symmetric top [24] molecules. Alternative methods such as optoelectric Sisyphus cooling [58] and Zeeman–Sisyphus deceleration [59] of polyatomic molecules have also been demonstrated. Briefly, in a type-II cycling scheme with more ground than excited sublevels, dark states exist. Molecules travelling at a velocity v through a standing wave formed by counter-propagating, near-resonant laser beams lose kinetic energy as they travel up potential hills that arise from spatially varying AC Stark shifts. At the top of the hill where the intensity is highest, molecules absorb the near-resonant photons and rapidly decay to a dark state, finding themselves at the bottom of the hill. If the magnetic field induced remixing rate is matched to the propagation time along the standing wave, $\lambda/(4v)$, the molecules return to the bright state and can climb up the potential hill again. This process repeats multiple times, leading to cooling. The opposite effect of Sisyphus heating can be generated by using a red-detuned laser (see figure 5 in the appendix and reference [60] for details).

We perform Sisyphus cooling and heating by allowing the laser beam in a multi-pass configuration to overlap between adjacent passes. In order to achieve higher intensities, we keep the laser beam waist relatively small. This leads to substantial beam expansion as the beam propagates. We rely on this expansion after ∼16 passes to create sufficient overlap for a standing wave. We estimate a peak intensity of ∼200 mW cm^{-2} for one beam within a 5 cm long interaction region (see appendix D). We apply a magnetic field $\vec{B}$ perpendicular to both the molecular beam and the laser wave vector $\vec{k}$, and tune the linear laser polarization to maximize R_{sc}. When optimized, we observe Sisyphus cooling at a detuning of +20 MHz as a visible compression of the width of the molecular distribution and also a slight enhancement in the on-axis molecule number (figure 4(a)). When the detuning is switched to −20 MHz, we instead see an increase in the molecular width and the emergence of bimodality near the center, a tell-tale sign of Sisyphus heating. We fit each trace to a 1D Gaussian function to obtain the $1/e$ cloud radius σ (see appendix D).

We perform optical Bloch equation (OBE) simulations of the internal states of the molecule in order to estimate the Sisyphus force. Details of the simulation can be found in references [60, 61] and in appendix D. Briefly, we account for 12 ground states and four excited states. We let these molecular states evolve under the OBEs. The force is calculated once the excited state population has reached steady state. Next, we perform Monte Carlo (MC) simulations of individual trajectories as the molecules travel through the interaction region and arrive in the detection region. The spatial distribution from the MC simulation can be compared to the measured camera images. In addition, the associated velocity distribution gives us access to the beam transverse temperature. Furthermore, we consider the full possible range of the standing wave intensity which determines the magnitude of the Sisyphus effect, and use this range to estimate the simulation uncertainty.

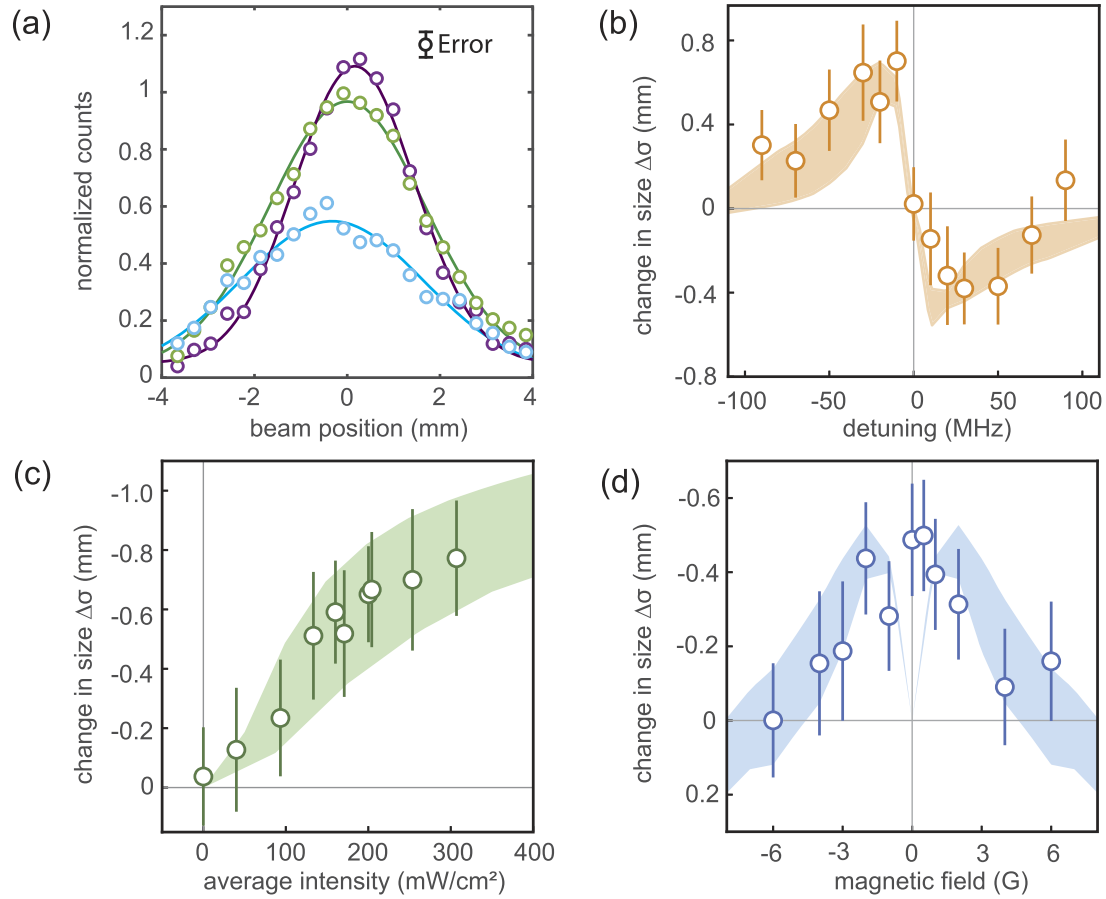

Figure 4. Magnetically assisted Sisyphus effect in CaH. (a) Molecular beam profiles obtained for an unperturbed beam (green), Sisyphus cooled beam (purple) at $\delta = +20$ MHz, and Sisyphus heated beam (blue) at $\delta = -20$ MHz. The y-axis is normalized to the unperturbed beam maximum and no other scale factors are used. Lines are fits to a 1D Gaussian function to obtain the $1/e$ cloud radius σ. The increase in on-axis molecule number seen in the cooling configuration is a clear signature of Sisyphus cooling. Statistical error for each point is represented by the bar on top right and is depicted separately for clarity. (b) Change in σ as a function of detuning, where $\Delta\sigma > 0$ implies heating and vice versa. The detuning is applied globally to each spin-rotation and hyperfine addressing lasers. The data was taken at an intensity of 200 mW cm^{-2}. The band represents the result of OBE and MC simulations for our experimental system. (c) Change in beam size $\Delta\sigma$ as a function of laser intensity. Detuning has been fixed at $\delta = +20$ MHz. We do not saturate the Sisyphus cooling effect even at the largest available laser intensity ($\sim$ 300 mW cm^{-2}). The simulations shown as a band suggest that an intensity of >600 mW cm^{-2} is required for saturation. (d) Change in beam size $\Delta\sigma$ as a function of magnetic field strength. Detuning is $\delta = +20$ MHz and intensity is 200 mW cm^{-2}. Maximum cooling is seen for $B \approx 1$ G. Note that the scattering rate is maximized at $B \approx 3$ G. The Sisyphus effect is expected to be nulled at $B = 0$, but due to the presence of the Earth's magnetic field and the low laser intensity we do not resolve the dip. The simulation shows the same behavior. The bands shown in simulations encompass the spatial variation in laser intensity we expect in the experiment. Each point is a result of 200 repetitions of the experiment, and the experimental error bars are standard errors of Gaussian fitting.

We characterize the Sisyphus effect in our experiment as a function of three parameters: detuning δ, intensity I, and magnetic field strength B (figures 4(b)–(d)). To quantify the cooling effect, we plot the change in cloud radius, $\Delta\sigma$, measured in mm. To minimize systematic effects, we take one molecule image with the Sisyphus laser beams on in one ablation pulse, followed by one molecule image with them off in the subsequent ablation pulse. This allows us to account for drifts in the ablation yield and beam velocity. We repeat this process for 200 shots to obtain the signal-to-noise ratio depicted in figure 4. We observe the expected Sisyphus behavior with detuning that is opposite of the Doppler effect: red-detuned heating and blue-detuned cooling. We additionally observe that the Sisyphus effect persists for detunings up to $\pm$50 MHz (figure 4(b)). We next measure the dependence on the laser intensity by varying the laser power while keeping the detuning fixed at $\delta = +20$ MHz. We note that we do not reach saturation of Sisyphus cooling at our maximum available laser intensity, although we expect to be in the saturated regime for photon scattering. This is due to the fact that the depth of the potential hill that quantifies the energy loss per cycle during Sisyphus cooling has a stronger dependence on the degree of overlap between adjacent beams than on the peak laser intensity. From the simulations, we predict that saturation can be expected for intensities above 600 mW cm^{-2} (figure 4(c)). At the intensity where we see the largest cooling effect, we estimate that the transverse temperature of the molecular beam is reduced from 12.2(1.2) mK to 5.7(1.1) mK while scattering 140^{+400}_{-60} photons. Lastly, we measure the dependence on magnetic field strength at a fixed

detuning ($\delta = +20$ MHz) and intensity (200 mW cm^{-2}). The magnetically assisted Sisyphus effect should operate at non-zero magnetic fields, and at our low laser intensities the peak is expected at ∼1 G as corroborated by simulations (figure 4(d)). Since the Earth's field is not cancelled in the experiment, we do not detect a clear dip around $B = 0$. Nevertheless, we can be certain that Sisyphus cooling is observed here, since maximum photon scattering occurs at $B \sim 3$ G.

6. Conclusion

In conclusion, we have characterized the dynamics of a cryogenic beam of CaH and experimentally measured the VBRs to the first three vibrational levels. We estimate that repumping the $v'' = 1$ and 2 vibrational states should allow us to scatter the $\sim 2 \times 10^4$ photons needed to slow the molecular beam to within the MOT capture velocity. We have demonstrated an ability to scatter ∼200 photos at a rate of $\sim 1.6 \times 10^6$ photons s^{-1} on the $A \leftarrow X$ transition while repumping the first excited vibrational state through the $B \leftarrow X(v'' = 1)$ transition. This scattering rate implies that, with an additional $v'' = 2$ repumping laser, we should be capable of slowing the molecular beam to within the MOT capture range in ∼20 ms. Finally we have demonstrated a sub-Doppler cooling mechanism on a CaH beam, reducing the transverse temperature from 12.2(1.2) mK to 5.7(1.1) mK while only scattering 140 photons via the magnetically assisted Sisyphus effect. Thus we have established that CaH molecules are amenable to further laser cooling. Once these molecules are cooled and trapped in a MOT, they could be used as a precursor for producing dilute ultracold hydrogen via photodissociation, for high-precision fundamental measurements.

Acknowledgments

We thank B Iritani, E Tiberi, and K H Leung for providing a stable laser referenced to the $1S_0 \rightarrow 3P_1$ transition in Sr, which was used for wavemeter calibration. We thank K Wenz, O Grasdijk, and C Hallas for fruitful discussions on OBE simulations. This work was supported by the W. M. Keck Foundation Grant CU19-2058, ONR Grant N00014-21-1-2644, and AFOSR MURI Grant FA9550-21-1-0069.

Data availability statement

The data that support the findings of this study are available upon reasonable request from the authors.

Appendix A. Laser configuration

For the $A \leftarrow X(v'' = 0)$ transition at 695 nm, we use two home-built external cavity diode lasers (ECDLs) separated by ∼2 GHz to address the $J = 1/2$ and $J = 3/2$ manifolds. Each ECDL is then passed through an acousto-optic modulator to generate two frequencies separated by the hyperfine splitting of the corresponding J-manifold (54 MHz for $J = 1/2$ and 101 MHz for $J = 3/2$, figure 1(d)). The resulting four frequencies are used to individually seed four injection-locked amplifiers (ILAs). Laser beams from the ILAs corresponding to a single J-manifold are first combined with orthogonal linear polarizations on a polarizing beam splitter, and then the two J-manifolds are combined on a 50:50 beam splitter. Hence a single $\lambda/2$-waveplate is sufficient to determine the polarization of each frequency component. The combined beam is spatially overlapped with light addressing the $B \leftarrow X(v'' = 1)$ repump transition at 690 nm using a narrow-band dichroic filter (FF01-690/8-25). Each repump transition is addressed with light produced by two ECDLs, each seeding one ILA and addressing a J-manifold. The hyperfine sidebands are added to the seed light via electro-optic modulators (EOMs), resonant at ∼50 MHz and using different order Bessel functions. In total, this laser setup is capable of providing 150 mW of $A \leftarrow X(v'' = 0)$ cooling light and 110 mW of $B \leftarrow X(v'' = 1)$ repumping light propagating from the same fiber. To achieve the maximum intensity for Sisyphus experiments, an additional 150 mW of cooling light was added to the system though a separate fiber. This additional cooling light is derived from the same laser source and results from the combination of different frequency components using beam splitters (figure 5(c)). After cooling we repump any leftover $v'' = 1$ population to $v'' = 0$ using 40 mW of repump light in the cleanup region. Detection is performed on the $B \leftarrow X(v'' = 0)$ transition by using two ECDLs at 635 nm addressing the two J-manifolds, with the hyperfine sidebands added via EOMs. Since 60 mW of light with 1.2 mm $1/e^2$ radius is sufficient for detection, no ILAs are used. EMCCD in the detection region is triggered at 0.5 ms after ablation, and exposure time is set to 7 ms.

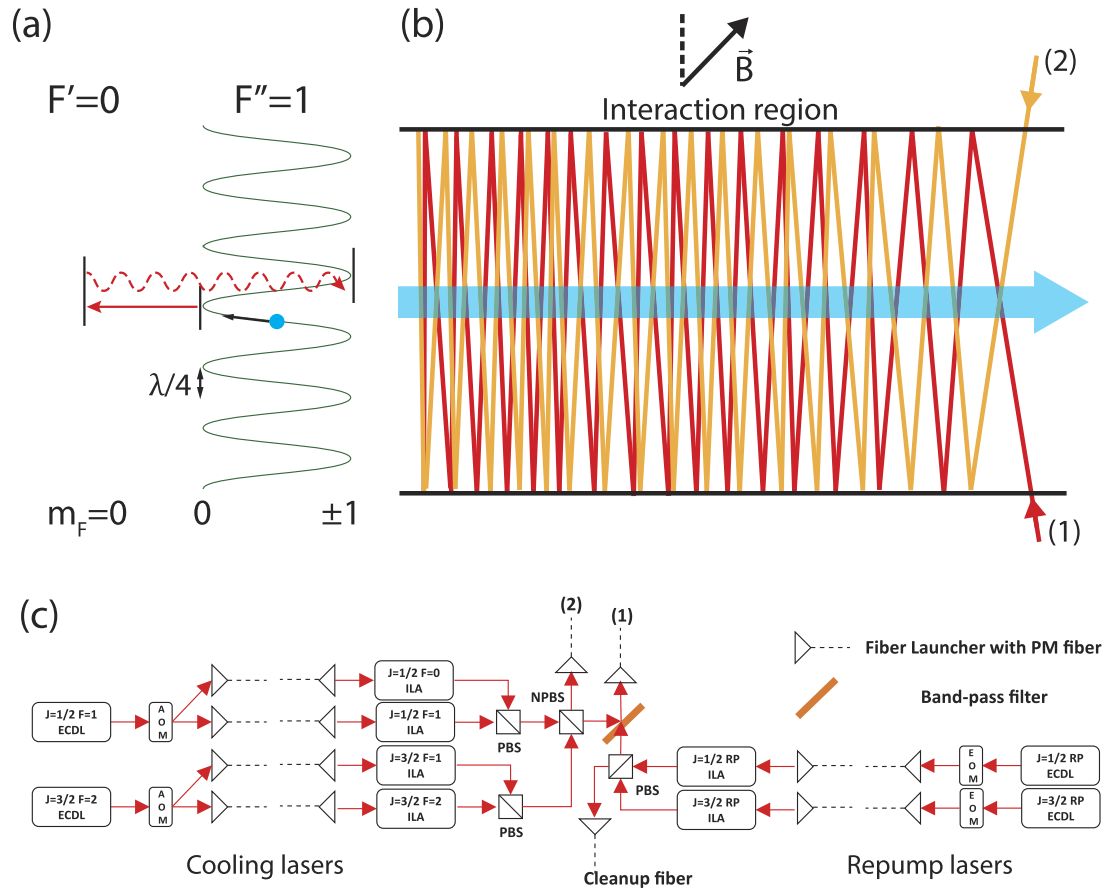

Figure 5. Laser configuration for Sisyphus cooling. (a) Schematic of the Sisyphus cooling process in the $F' = 0 \leftarrow F'' = 1$ configuration. The standing wave formed by the overlap of the blue detuned, linearly polarized laser beam leads to a Stark-shifted potential hill. As a molecule (blue sphere) travels up this potential hill, it loses energy and is optically pumped to the excited state at the top of the hill. The spontaneous decay brings the molecule back to the dark ground state. Precession around an external magnetic field ($\vec{B}$) mixes the ground sublevels and brings the molecule back into the bright state to continue the process. (b) Schematic of the interaction region. Blue arrow denotes molecular beam direction. Two separate laser beams are used to form independent standing waves. The first laser beam (1) containing both $A \leftarrow X(v'' = 0)$ and $B \leftarrow X(v'' = 1)$ frequencies enters the interaction region near the end and is retroreflected such that the spacing between adjacent passes gradually decreases. After 16 passes, the adjacent passes have sufficient overlap to form a standing wave. The second laser beam (2) only addresses $A \leftarrow X(v'' = 0)$ and can be added to obtain higher average intensities. (c) Arrangement of ECDLs and ILAs used to generate the cooling and repump light and their combination. Some components such as mirrors and waveplates are omitted for simplicity. Note that the method of combination leads to an equal split of the cooling light into two fibers (1) and (2).

Appendix B. Molecular beam flux estimation

Here we discuss the estimation of the molecular beam flux. In the experiment, we detect the molecules using the $B(v' = 0) \leftarrow X(v'' = 0)$ transition at 635 nm and collect the scattered photons with an EMCCD camera (Andor iXon Ultra 888). We use the following equation to convert the camera counts to the total energy of the collected photons per manufacturer:

$$E_{\mathrm{ph}} = \frac{\mathrm{Cts}}{g} \times \frac{S}{Q} \times 3.65\ \mathrm{eV}, \tag{9}$$

where Cts, g, S and Q denote total camera counts, EM gain, CCD sensitivity and quantum efficiency, respectively. We can then estimate the molecule number as

$$N_{\mathrm{mol}} = \frac{E_{\mathrm{ph}}/h\nu}{\eta \times R_{\mathrm{sc}} t}. \tag{10}$$

The collection efficiency of our imaging system η is around 1% and constitutes the highest source of uncertainty due to our inability to directly measure it. The interaction time t is determined using the laser beam waist and a $\sim$250 m s^{-1} peak velocity.

Table 2. Measured parameter values that are used to calculate VBRs and FCFs for CaH given in section 3.

$A^2\Pi_{1/2}\, q_{01}$	Value	Error	$A^2\Pi_{1/2}\, q_{02}$	Value	Error
R_0	1.575	0.013	R_0	1.363	0.015
R_1	0.0410	0.0017	R_2	0.0007	0.0005
$Q_{P_2,\lambda_{01}}/Q_{P_2,\lambda_{00}}$	0.73	0.04	$Q_{P_2,\lambda_{02}}/Q_{P_2,\lambda_{00}}$	0.167	0.008
$T_{F_3,\lambda_{01}}/T_{F_2,\lambda_{00}}$	1.17	0.06	$T_{F_3,\lambda_{02}}/T_{F_2,\lambda_{00}}$	1.15	0.06
q_{01}/q_{00}	**0.0306**	**0.0025**	q_{02}/q_{00}	**0.0025**	**0.0019**
$B^2\Sigma^+\, q_{01}$	Value	Error	$B^2\Sigma^+\, q_{02}$	Value	Error
R_0	5.83	0.05	R_0	5.83	0.03
R_1	0.0696	0.0021	R_2	0.0040	0.0005
$Q_{P_2,\lambda_{01}}/Q_{P_2,\lambda_{00}}$	0.86	0.05	$Q_{P_2,\lambda_{02}}/Q_{P_2,\lambda_{00}}$	0.56	0.03
$T_{F_3,\lambda_{01}}/T_{F_2,\lambda_{00}}$	1.01	0.04	$T_{F_3,\lambda_{02}}/T_{F_2,\lambda_{00}}$	1.00	0.05
q_{01}/q_{00}	**0.0137**	**0.0011**	q_{02}/q_{00}	**0.001 25**	**0.000 19**

Table 3. List of all dichroic filters used in the VBR and FCF measurements for CaH given in section 3. All filters are purchased from Semrock, except FL635-10 which is purchased from Thorlabs.

	F_1	F_2	F_3
$A^2\Pi_{1/2}\, q_{01}$	FF01-692/40-25	FF02-684/24-25	FF01-760/12-25
$A^2\Pi_{1/2}\, q_{02}$	FF01-692/40-25	FF02-684/24-25	FF01-840/12-25
$B^2\Sigma^+\, q_{01}$	FL635-10	FF01-630/20-25	FF01-690/8-25
$B^2\Sigma^+\, q_{02}$	FL635-10	FF01-630/20-25	FF01-760/12-25

Molecular beam flux is defined as the number of molecules detected per unit solid angle with respect to the cell aperture. With an estimation of the solid angle given the molecular beam size on the camera and the distance from the cell, we estimate our molecular beam flux to be $\sim 1 \times 10^{10}$ molecules/steradian/pulse.

Appendix C. VBR measurement

Here we present the details that factor into the calculation of A and B state VBRs (section 3). In general, $R_{\nu''}$, where $\nu'' = 0, 1, 2$, is the fitted ratio of two PMT time traces. The fitting time window is from 1 ms to 7 ms, and we use the data between 35 ms and 90 ms for background subtraction. We use the same fitting protocol for all $R_{\nu''}$ measurements. The ratio $R_{\nu''}$ is stable during data collection and only varies if the position of either PMT is altered.

The quantum efficiencies of PMTs are either experimentally measured or obtained from factory calibration results. We use the following expression to measure the quantum efficiency:

$$Q = \frac{\text{Cts}}{P/\hbar\omega}, \tag{11}$$

where Cts is the total number of PMT counts per second, P is the laser power incident into the PMT, and $\hbar\omega$ is the photon energy. Each PMT is placed into a black box, and an optical fiber carrying light directly points at the PMT active surface. To prevent saturation of the PMT, we insert calibrated neutral-density filters between the fiber and the PMT head. We measure Q at several different laser powers and fit to a line to obtain the PMT linear response. Eventually we measured Q at 635 nm, 690 nm and 695 nm, and find that our measured Q is within 5% of the manufacturer's specifications. However, due to the lack of available laser sources at the other fluorescence wavelengths, we employ the factory calibrated values for Q provided by the manufacturer, and assign a 5% error to them. We also directly measure the transmission efficiencies of all dichroic filters used for the experiment if a laser source is available, otherwise we use the manufacturer's specifications.

Table 2 shows all the measured values that are used in calculating VBRs and their errors, and table 3 lists the dichroic filters used for the measurement of VBRs.

Appendix D. OBE and MC simulations

We developed the OBE solver [60–63] using Python and Julia (via PyJulia). The source code can be found online[3]. We include 12 ground states of ($X^2\Sigma^+, \nu'' = 0, N'' = 1$) in Hund's case (b) and four excited states of ($A^2\Pi_{1/2}, \nu' = 0, J' = 1/2$) in Hund's case (a). We ignore another 12 states in the ($X^2\Sigma^+, \nu'' = 1, N'' = 1$) level, because the population in the vibrationally excited state is not significant in our experiment. The transition dipole moments are calculated with the help of a Matlab package[4] where a Hund's case (b) basis is projected onto a case (a) basis. We perform MC simulation of the classical trajectories of the cryogenic molecular beam[5]. We initialize 10^4 molecules at the exit of the 5 mm beam aperture described in section 2, and propagate them through the interaction region where they experience Sisyphus forces as described in section 5.

We combine the OBE and MC simulations as follows: at a given laser polarization and other experimental parameters, we perform a two-dimensional parameter sweep of velocity and laser intensity using the OBE simulation of the optical force. Then within the MC simulation, for each particle with a position and velocity, we perform a 2D interpolation to obtain the instantaneous force on the particle. In order to accurately model the spatial variation of intensity, we assume Gaussian beam propagation along with loss per pass due to imperfections. We measure the beam width before it enters the interaction region, and use the number of passes to estimate the traveling distance and calculate the laser beam waist. The beam waist $w(z)$ at a distance z is calculated as

$$w(z) = w(0)\sqrt{1 + (z/z_R)^2}, \tag{12}$$

where $z_R = \pi w(0)^2/\lambda$ is the Rayleigh range. We measure the spacing of the laser beams to convert from the spatial coordinate to the number of passes. We also observe a moderate power loss every time a laser beam passes through the chamber ($\sim$1.8%). Together, these provide us with a conversion from spatial position to local laser intensity. Molecules propagate through the interaction region and eventually exit to reach the detection region. We then plot the spatial distribution of molecules and perform a one-dimensional Gaussian fit to extract the width information. The fit function used for all experimental data as well as simulations is

$$y(r) = y(0) + A\exp(-(r - r_0)^2/(2\sigma^2)), \tag{13}$$

where σ is the $1/e$ radius of the cloud (figure 4(a)).

D.1. Assignment of simulation uncertainty

The main source of uncertainty in the simulations stems from our inability to measure the position and amplitude of the standing wave that gives rise to the Sisyphus effect. Although the multi-pass laser beams are distinguishable initially (i.e. do not overlap), after 16 passes they overlap significantly. This overlap region, where the standing wave is formed and Sisyphus forces act, covers $\sim$5 cm of the interaction length (figure 5(b)). In addition, it is challenging to estimate the beam waist within this region. We quantify this uncertainty by considering two situations: (1) the laser beams are tightly spaced and the effective overlap is long, and (2) the beams are loosely spaced and their overlap is small. For example, in figure 4(c), the simulation band ranges from a 5 cm overlap with 1 mm beam spacing, or a 4 cm overlap with 2 mm beam spacing. The same strategy is used in generating the simulation bands in figures 4(b) and (d) as well.

D.2. Laser intensity estimation

The intensity of a Gaussian laser beam is defined as $I = 2P/(\pi w^2)$ where I is the peak intensity, P is the total power, and w is the $1/e^2$ waist. We measure the laser beam power and waist before it enters the interaction region. The beam focus lies outside the interaction region. Then we estimate the peak intensity after the beam undergoes N passes using equation (12). Furthermore, since the beam overlap that can lead to a Sisyphus effect is between the beam aperture and $\sim$5 cm downstream, we denote the average intensity between 7 cm and 12 cm from the first pass of the laser beam that is coupled from the downstream side of the 12 cm long interaction region (figure 1(a)). This is how the x-axis of the experimental data in figure 4(c) is generated.

For the MC simulation, we define the average intensity from the local intensities experienced by each molecule as the molecular beam traverses the interaction region. We tabulate the local intensities

[3] github.com/QiSun97/OBE-Solver.

[4] github.com/QiSun97/Rabi_Matrix_Elements_Calculator.

[5] github.com/QiSun97/Cryogenic_Beam_Sisyphus_MC_Simulation.

experienced by all detected particles at the end of the simulation and calculate the median of the distribution to obtain the average intensity.

D.3. Transverse temperature estimation

We estimate the transverse temperature of the molecular beam as follows. Within the MC simulation, the only free parameter that allows us to match the detected spatial distribution is the transverse temperature that governs the transverse velocity distribution. The spatial distribution is assumed to be uniform at the 5 mm aperture, and the forward velocity is experimentally determined. Thus, we obtain a one-to-one correspondence of the molecular beam width to the transverse temperature of the beam. The unperturbed beam has a width of 3.11(14) mm, which corresponds to 12.2(1.2) mK, and the coldest beam has a width of 2.34(13) mm, which corresponds to 5.7(1.1) mK.

ORCID iDs

D Mitra https://orcid.org/0000-0002-2150-721X
T Zelevinsky https://orcid.org/0000-0003-3682-4901

References

[1] Raab E L, Prentiss M, Cable A, Chu S and Pritchard D E 1987 Trapping of neutral sodium atoms with radiation pressure *Phys. Rev. Lett.* **59** 2631–4
[2] Phillips W D 1998 Nobel lecture: laser cooling and trapping of neutral atoms *Rev. Mod. Phys.* **70** 721–41
[3] Bloch I, Dalibard J and Zwerger W 2008 Many-body physics with ultracold gases *Rev. Mod. Phys.* **80** 885–964
[4] Morgado M and Whitlock S 2021 Quantum simulation and computing with Rydberg-interacting qubits *AVS Quantum Sci.* **3** 023501
[5] Bothwell T, Kennedy C J, Aeppli A, Kedar D, Robinson J M, Oelker E, Staron A and Ye J 2022 Resolving the gravitational redshift across a millimetre-scale atomic sample *Nature* **602** 420–4
[6] Safronova M S, Budker D, DeMille D, Jackson Kimball D F, Derevianko A and Clark C W 2018 Search for new physics with atoms and molecules *Rev. Mod. Phys.* **90** 025008
[7] Tarbutt M R 2018 Laser cooling of molecules *Contemp. Phys.* **59** 356–76
[8] Andreev V *et al* (The ACME Collaboration) 2018 Improved limit on the electric dipole moment of the electron *Nature* **562** 355
[9] Cairncross W B and Ye J 2019 Atoms and molecules in the search for time-reversal symmetry violation *Nat. Rev. Phys.* **1** 510
[10] Augenbraun B, Lasner Z, Frenett A, Sawaoka H, Miller C, Steimle T and Doyle J M 2020 Laser-cooled polyatomic molecules for improved electron electric dipole moment searches *New J. Phys.* **22** 022003
[11] Park J W, Yan Z Z, Loh H, Will S A and Zwierlein M W 2017 Second-scale nuclear spin coherence time of ultracold ^{23}Na ^{40}K molecules *Science* **357** 372–5
[12] Blackmore J A *et al* 2019 Ultracold molecules for quantum simulation: rotational coherences in CaF and RbCs *Quantum Sci. Technol.* **4** 014010
[13] Sawant R, Blackmore J A, Gregory P D, Mur-Petit J, Jaksch D, Aldegunde J, Hutson J M, Tarbutt M R and Cornish S L 2020 Ultracold polar molecules as qudits *New J. Phys.* **22** 013027
[14] Hazzard K R A *et al* 2014 Many-body dynamics of dipolar molecules in an optical lattice *Phys. Rev. Lett.* **113** 195302
[15] Hutzler N R, Lu H-I and Doyle J M 2012 The buffer gas beam: an intense, cold, and slow source for atoms and molecules *Chem. Rev.* **112** 4803–27
[16] Barry J F, Shuman E S and DeMille D 2011 A bright, slow cryogenic molecular beam source for free radicals *Phys. Chem. Chem. Phys.* **13** 18936–47
[17] Shuman E S, Barry J F and DeMille D 2010 Laser cooling of a diatomic molecule *Nature* **467** 820–3
[18] Truppe S, Williams H J, Hambach M, Caldwell L, Fitch N J, Hinds E A, Sauer B E and Tarbutt M R 2017 Molecules cooled below the Doppler limit *Nat. Phys.* **13** 1173–6
[19] Anderegg L *et al* 2017 Radio frequency magneto-optical trapping of CaF with high density *Phys. Rev. Lett.* **119** 103201
[20] Collopy A L, Ding S, Wu Y, Finneran I A, Anderegg L, Augenbraun B L, Doyle J M and Ye J 2018 3D magneto-optical trap of yttrium monoxide *Phys. Rev. Lett.* **121** 213201
[21] McNally R L, Kozyryev I, Vazquez-Carson S, Wenz K, Wang T and Zelevinsky T 2020 Optical cycling, radiative deflection and laser cooling of barium monohydride (^{138}Ba^{1}H) *New J. Phys.* **22** 083047
[22] Kozyryev I, Baum L, Matsuda K, Augenbraun B L, Anderegg L, Sedlack A P and Doyle J M 2017 Sisyphus laser cooling of a polyatomic molecule *Phys. Rev. Lett.* **118** 173201
[23] Vilas N B, Hallas C, Anderegg L, Robichaud P, Winnicki A, Mitra D and Doyle J M 2021 Magneto-optical trapping and sub-Doppler cooling of a polyatomic molecule (arXiv:2112.08349)
[24] Mitra D, Vilas N B, Hallas C, Anderegg L, Augenbraun B L, Baum L, Miller C, Raval S and Doyle J M 2020 Direct laser cooling of a symmetric top molecule *Science* **369** 1366–9
[25] Tiesinga E, Mohr P J, Newell D B and Taylor B N 2021 CODATA recommended values of the fundamental physical constants: 2018 *Rev. Mod. Phys.* **93** 025010
[26] Biraben F 2009 Spectroscopy of atomic hydrogen *Eur. Phys. J. Spec. Top.* **172** 109–19
[27] Fried D G, Killian T C, Willmann L, Landhuis D, Moss S C, Kleppner D and Greytak T J 1998 Bose–Einstein condensation of atomic hydrogen *Phys. Rev. Lett.* **81** 8311
[28] Cesar C L, Fried D G, Killian T C, Polcyn A D, Sandberg J C, Yu I A, Greytak T J, Kleppner D and Doyle J M 1996 Two-photon spectroscopy of trapped atomic hydrogen *Phys. Rev. Lett.* **77** 255–8
[29] Ahmadi M *et al* 2017 Observation of the 1*S*–2*S* transition in trapped antihydrogen *Nature* **541** 506–10
[30] Parthey C G *et al* 2011 Improved measurement of the hydrogen 1*S*–2*S* transition frequency *Phys. Rev. Lett.* **107** 203001

[31] Grinin A, Matveev A, Yost D C, Maisenbacher L, Wirthl V, Pohl R, Hänsch T W and Udem T 2020 Two-photon frequency comb spectroscopy of atomic hydrogen *Science* **370** 1061–6

[32] Brandt A D, Cooper S F, Rasor C, Burkley Z, Matveev A and Yost D C 2022 Measurement of the $2S_{1/2}$–$8D_{5/2}$ transition in hydrogen *Phys. Rev. Lett.* **128** 023001

[33] Raizen M G 2009 Comprehensive control of atomic motion *Science* **324** 1403–6

[34] Lane I C 2015 Production of ultracold hydrogen and deuterium via Doppler-cooled Feshbach molecules *Phys. Rev.* A **92** 022511

[35] Jones S A 2022 An ion trap source of cold atomic hydrogen via photodissociation of the BaH^+ molecular ion *New J. Phys.* **24** 023016

[36] Rosa M D 2004 Laser-cooling molecules: concept, candidates, and supporting hyperfine-resolved measurements of rotational lines in the A–$X(0, 0)$ band of CaH *Eur. Phys. J.* D **31** 395–402

[37] Lu H-I, Rasmussen J, Wright M J, Patterson D and Doyle J M 2011 A cold and slow molecular beam *Phys. Chem. Chem. Phys.* **13** 18986–90

[38] Weinstein J D, deCarvalho R, Guillet T, Friedrich B and Doyle J M 1998 Magnetic trapping of calcium monohydride molecules at millikelvin temperatures *Nature* **395** 148–50

[39] Stuhl B K, Sawyer B C, Wang D and Ye J 2008 Magneto-optical trap for polar molecules *Phys. Rev. Lett.* **101** 243002

[40] Barry J F, McCarron D J, Norrgard E B, Steinecker M H and DeMille D 2014 Magneto-optical trapping of a diatomic molecule *Nature* **512** 286–9

[41] Lim J, Almond J R, Trigatzis M A, Devlin J A, Fitch N J, Sauer B E, Tarbutt M R and Hinds E A 2018 Laser cooled YbF molecules for measuring the electron's electric dipole moment *Phys. Rev. Lett.* **120** 123201

[42] Kozyryev I, Steimle T C, Yu P, Nguyen D-T and Doyle J M 2019 Determination of CaOH and $CaOCH_3$ vibrational branching ratios for direct laser cooling and trapping *New J. Phys.* **21** 052002

[43] Gao Y and Gao T 2014 Laser cooling of the alkaline-earth-metal monohydrides: insights from an *ab initio* theory study *Phys. Rev.* A **90** 052506

[44] Cheng X, Bai J, Yin J-P and Wang H-L 2015 Franck–Condon factors and band origins for MgH in the $A^2\Pi$–$X^2\Sigma^+$ system *Chin. J. Chem. Phys.* **28** 253–6

[45] Tarallo M G, Iwata G Z and Zelevinsky T 2016 BaH molecular spectroscopy with relevance to laser cooling *Phys. Rev.* A **93** 032509

[46] Ramanaiah M V and Lakshman S V J 1982 True potential energy curves and Franck–Condon factors of a few alkaline earth hydrides *Physica B+C* **113** 263–70

[47] Pathak A N and Singh P D 1966 Franck–Condon factors and r-centroids of the CaH (B–X) band system *Proc. Phys. Soc.* **87** 1008–9

[48] Hendricks R J, Holland D A, Truppe S, Sauer B E and Tarbutt M R 2014 Vibrational branching ratios and hyperfine structure of ^{11}BH and its suitability for laser cooling *Front. Phys.* **2** 51

[49] Liu M, Pauchard T, Sjödin M, Launila O, van der Meulen P and Berg L-E 2009 Time-resolved study of the $A^2\Pi$ state of CaH by laser spectroscopy *J. Mol. Spectrosc.* **257** 105–7

[50] Berg L-E, Ekvall K and Kelly S 1996 Radiative lifetime measurement of vibronic levels of the $B^2\Sigma^+$ state of CaH by laser excitation spectroscopy *Chem. Phys. Lett.* **257** 351–5

[51] Shayesteh A, Ram R S and Bernath P F 2013 Fourier transform emission spectra of the $A^2\Pi$–$X^2\Sigma^+$ and $B^2\Sigma^+$–$X^2\Sigma^+$ band systems of CaH *J. Mol. Spectrosc.* **288** 46–51

[52] Norrgard E B, McCarron D J, Steinecker M H, Tarbutt M R and DeMille D 2016 Submillikelvin dipolar molecules in a radio-frequency magneto-optical trap *Phys. Rev. Lett.* **116** 063004

[53] Anderegg L, Augenbraun B L, Bao Y, Burchesky S, Cheuk L W, Ketterle W and Doyle J M 2018 Laser cooling of optically trapped molecules *Nat. Phys.* **14** 890–3

[54] Caldwell L, Devlin J A, Williams H J, Fitch N J, Hinds E A, Sauer B E and Tarbutt M R 2019 Deep laser cooling and efficient magnetic compression of molecules *Phys. Rev. Lett.* **123** 033202

[55] Ding S, Wu Y, Finneran I A, Burau J J and Ye J 2020 Sub-Doppler cooling and compressed trapping of YO molecules at μK temperatures *Phys. Rev.* X **10** 021049

[56] Emile O, Kaiser R, Gerz C, Wallis H, Aspect A and Cohen-Tannoudji C 1993 Magnetically assisted Sisyphus effect *J. Physique II* **3** 1709–33

[57] Sheehy B, Shang S-Q, van der Straten P, Hatamian S and Metcalf H 1990 Magnetic-field-induced laser cooling below the Doppler limit *Phys. Rev. Lett.* **64** 858–61

[58] Zeppenfeld M, Englert B G U, Glöckner R, Prehn A, Mielenz M, Sommer C, van Buuren L D, Motsch M and Rempe G 2012 Sisyphus cooling of electrically trapped polyatomic molecules *Nature* **491** 570–3

[59] Augenbraun B L, Frenett A, Sawaoka H, Hallas C, Vilas N B, Nasir A, Lasner Z D and Doyle J M 2021 Zeeman–Sisyphus deceleration of molecular beams *Phys. Rev. Lett.* **127** 263002

[60] Devlin J A and Tarbutt M R 2016 Three-dimensional Doppler, polarization-gradient, and magneto-optical forces for atoms and molecules with dark states *New J. Phys.* **18** 123017

[61] Devlin J A and Tarbutt M R 2018 Laser cooling and magneto-optical trapping of molecules analyzed using optical Bloch equations and the Fokker–Planck–Kramers equation *Phys. Rev.* A **98** 063415

[62] Wenz K 2021 Nuclear Schiff moment search in thallium fluoride molecular beam: rotational cooling *PhD Thesis* Columbia University

[63] Wenz K, Kozyryev I, McNally R L, Aldridge L and Zelevinsky T 2020 Large molasses-like cooling forces for molecules using polychromatic optical fields: a theoretical description *Phys. Rev. Res.* **2** 043377